


A tunable path-separated electron interferometer with an amplitude-dividing grating beamsplitter

Cite as: Appl. Phys. Lett. **113**, 233102 (2018); <https://doi.org/10.1063/1.5051380>

Submitted: 08 August 2018 . Accepted: 07 November 2018 . Published Online: 05 December 2018

Fehmi S. Yasin , Ken Harada, Daisuke Shindo, Hiroyuki Shinada, Benjamin J. McMorran, and Toshiaki Tanigaki



View Online



Export Citation



CrossMark

ARTICLES YOU MAY BE INTERESTED IN

[Depth sensitive imaging of graphene with an atomic resolution microscope](#)

Applied Physics Letters **113**, 233101 (2018); <https://doi.org/10.1063/1.5053926>

[Impact of electrodes on the extraction of shift current from a ferroelectric semiconductor SbSI](#)

Applied Physics Letters **113**, 232901 (2018); <https://doi.org/10.1063/1.5055692>

[Remote heteroepitaxy across graphene: Hydrothermal growth of vertical ZnO microrods on graphene-coated GaN substrate](#)

Applied Physics Letters **113**, 233103 (2018); <https://doi.org/10.1063/1.5064542>

Lock-in Amplifiers
up to 600 MHz



Watch



A tunable path-separated electron interferometer with an amplitude-dividing grating beamsplitter

Fehmi S. Yasin,^{1,2} Ken Harada,³ Daisuke Shindo,^{3,4} Hiroyuki Shinada,² Benjamin J. McMorran,^{1,a)} and Toshiaki Tanigaki²

¹Department of Physics, 120 Willamette Hall, 1371 E 13th Avenue, Eugene, Oregon 97403, USA

²Research and Development Group, Hitachi Ltd., Hatoyama 350-0321, Japan

³RIKEN Center for Emergent Matter Science (CEMS), Hatoyama 350-0321, Japan

⁴Institute of Multidisciplinary Research for Advanced Materials, Tohoku University, Sendai 980-8577, Japan

(Received 8 August 2018; accepted 7 November 2018; published online 5 December 2018)

We demonstrate a tunable path-separated electron interferometer using a single amplitude-dividing beamsplitter to prepare multiple spatially isolated, coherent electron probe beams. We place four electrostatic bi-prisms in the optical column of a scanning transmission electron microscope (STEM) to achieve path separations of up to 25 μm , the largest demonstrated within amplitude-division electron interferometers while maintaining fringe visibility of the directly observed interference fringes at the detector. We characterize the fringe visibility of this setup over a range of path separations and perform STEM holography to reconstruct the full object wave of a fabricated Si ramp test phase object. We report a quantitative object-wave measurement in this configuration and confirm with an independent off-axis electron holography measurement. This experimental design can potentially be applied to high-resolution phase imaging and fundamental physics experiments, such as an exploration of the electron wave packet coherence length and the Aharonov-Bohm effect. © 2018 Author(s). All article content, except where otherwise noted, is licensed under a Creative Commons Attribution (CC BY) license (<http://creativecommons.org/licenses/by/4.0/>).

<https://doi.org/10.1063/1.5051380>

Electron interferometry has been utilized to probe fundamental physics and provide object wave imaging since Dennis Gabor hypothesized an “electron interference microscope” in 1948.¹ Electrons offer different advantages from their optical counterparts. Electrons are massive, yet can still be accelerated to relativistic speeds. Their charge allows for a strong coupling to electromagnetic fields and their shorter De Broglie wavelength provides electron interferometers with higher resolving power, making them potent tools for materials research and the exploration of fundamental physics.

Marton *et al.* built the first electron interferometer using amplitude-dividing polycrystalline epitaxially grown copper membrane diffraction gratings in 1953² and Möllenstedt and Düker followed close behind with wavefront-dividing electron biprisms in 1955.³ The latter technology proved to be quite versatile allowing Lichte *et al.* to establish electron holography as a trusted technique for either high precision imaging^{4–8} or probing basic physics.^{9–11} Tanigaki *et al.* expanded on this setup through split-illumination electron holography (SIEH),¹² which boasts an additional two biprisms for pre-specimen beam splitting. This method utilizes the electron biprism to tune the path separation at the specimen plane, although with two notable difficulties. First, SIEH uses plane wave illumination incident on the specimen, similar to normal off-axis electron holography. This requires custom beam-blocking apertures in order to measure a field-of-interest surrounding a beam-sensitive specimen.¹³ Second, although it remains a useful technology, Möllenstedt electron

biprisms require wide, coherent incident beams when employed as a beamsplitter, thus demanding a highly coherent beam.

One way to alleviate this coherence requirement is by using electron diffraction grating beamsplitters. Similar to the original beamsplitter reported by Marton *et al.*, diffraction gratings are advantageous because they are amplitude-dividing beamsplitters, which create copies of the original wavefront propagating in different directions. They have the advantage that only a few grating bars, typically tens to hundreds of nanometers in pitch, must be coherently illuminated in order to maintain fringe visibility in the interference pattern.^{14–16} This decreases the coherence width requirements by at least an order-of-magnitude when compared to current biprism beamsplitters and could potentially allow implementation of this interferometer without highly coherent electron source guns such as cold field-emission guns or Schottky sources, for example. Holographic diffraction gratings have been developed by several groups^{17–22} and have been employed as beamsplitters in a couple of path separated electron interferometers^{17,23} and in a proposed electron interferometer with path separations of 10^{-2} m.²⁴ Using current focused ion beam (FIB) engineering techniques, we fabricated gratings that form electron diffraction orders (henceforth called p_n for the n_{th} order) with a spatial separation of hundreds of nanometers at the Lorentz sample plane, located in a field-free region above the objective lens useful for imaging magnetic materials, and tens of nanometers at the high-resolution sample plane in a commercial transmission electron microscope (TEM) configured in the scanning (STEM) mode.²³

In this article, we combine an amplitude-dividing beamsplitter with the versatility of electrostatic biprisms to

^{a)} Author to whom correspondence should be addressed: mcmorran@uoregon.edu

create a tunable path-separated electron interferometer. Harvey *et al.* and Yasin *et al.* previously developed and demonstrated the full object wave measurement using STEM holography (STEMH).^{25,26} Here, we use this interferometer to perform flexible STEM holography (fSTEMH), where we have increased flexibility via the tunability of the path separation. This increases the field of view of STEMH and opens the door to fundamental physics experiments as well as microscopy applications requiring large path-separations and localized-probe.

This interferometer was setup within a Hitachi HF-3000X TEM equipped with a cold field-emission gun and several positionable electrostatic biprism wires placed both pre- and post-specimen. As illustrated in Fig. 1, the input electron wave diffracts through a diffraction grating with pitch $d=190$ nm and is focused into electron probes with an estimated convergence semi-angle of 0.2 mrad and hundreds of nanometers spatial separation at the Lorentz specimen plane using a two-condenser lens illumination system. Note that the original probe separation at the specimen plane depends on both the physical pitch of the diffraction grating and the setup of the microscope lens system and biprisms. These gratings can be fabricated so that the amplitude of the diffraction orders other than p_{-1} , p_0 , and p_{+1} is approximately negligible.²⁰

Four BPs are positioned along the optical axis and are tuned such that the diffraction probes straddle the three BPs located further down the microscope column. The probes are

focused onto the first bi-prism (BP1), which blocks p_0 entirely. This increases the signal-to-noise of the desired frequency fringes for two reasons. First, the probe intensity $|p_0|^2 > |p_{n>0}|^2$, so it contains the majority of inelastically scattered electrons from the grating. Second, when p_{-1} , p_0 , and p_{+1} are all utilized, the amplitude $|p_0|$ may be large enough for a non-negligible interference signal with $p_{\pm 2}$, adding noise.²⁶ Blocking p_0 removes these two sources of noise. While the diffracted probes may contain inelastic scattering, Shiloh *et al.* have shown that a 200 nm thick SiN membrane has a ratio of elastic to inelastically scattered electrons of ≈ 0.66 , with most of the inelastically scattered electrons contained in the long tails of the probes.²⁷ Since our diffraction grating is 75 nm thick, we expect the proportion of inelastically scattered electrons to be even lower. BP1 changes the overlap of the interference fringe discs while BP2 tunes the path separation of the probes in the specimen plane. BP1 and BP2 are tuned such that the remaining diffraction probes straddle BP2 and spatially separate at the specimen plane to a desired value. p_{-1} interacts with the phase-object while p_{+1} passes through vacuum. The image of the grating is then focused onto BP3, with two spatially separated images formed due to the voltage bias engaged in BP1. We tuned this voltage so that the images straddle BP3. We then engage BP3 to decrease the spatial separation of the diffraction probes focused onto BP4 in the reciprocal plane, affectively increasing the fringe spacing in the image plane at the detector. Finally, we engage BP4 to

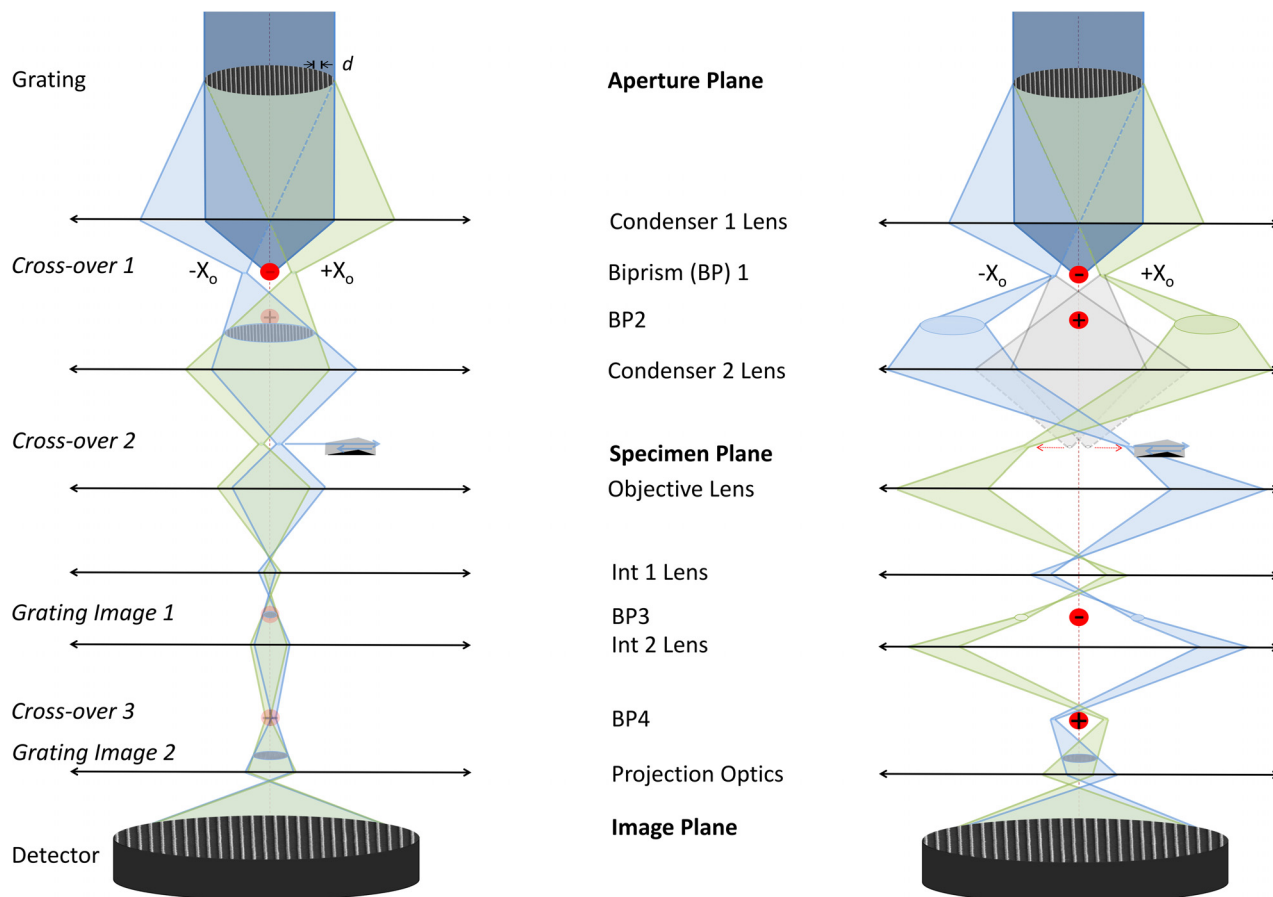


FIG. 1. Experimental setup for a tunable path-separated interferometer. The right-hand-side illustrates the change in path with the biprisms engaged.

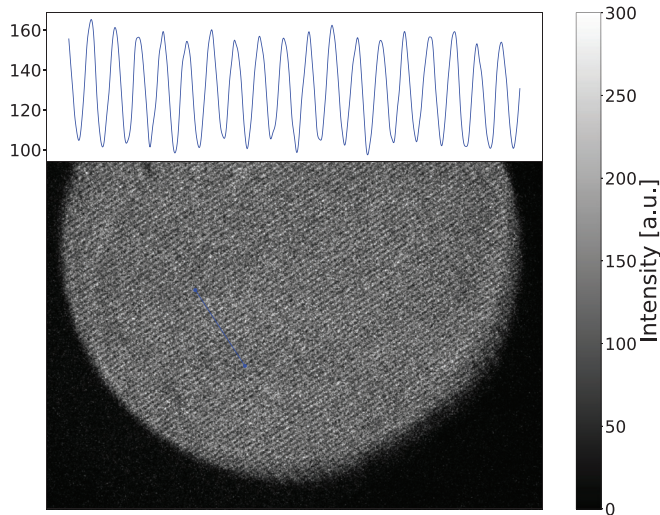


FIG. 2. Interference fringes at the detector. The inset is the mean of 400 1D slices of the interference fringe pattern.

overlap the grating images onto the detector, a Gatan US4000 charge-coupled device (CCD) that records the interference pattern, shown in Fig. 2.

For use as an easily characterizable phase object specimen, we placed Si on a Mo substrate with W as an adhesion layer using FIB microsampling.²⁸ We nanofabricated the Si to form a linear phase ramp, increasing from vacuum to ≈ 30 rad, (≈ 360 nm thick) over ≈ 1.2 μm on one side and decreases linearly with twice the gradient on the other side, or $-50 \frac{\text{rad}}{\mu\text{m}}$. We performed both fSTEMH with a path separation of $\Delta x = 5$ μm and off-axis electron holography on this test specimen. As shown in Fig. 3, fSTEMH accurately measures the phase profile of the Si, as compared to off-axis electron holography.

The microscope we used was not outfitted with a native STEM mode or aberration correction, so the probe width at the specimen plane limits our resolution to ≈ 45 nm. A dedicated STEM can improve this resolution, and STEM holography has been previously demonstrated at subnanometer resolution.²⁶ We adjusted our scan step size to be as large as the probe width to decrease acquisition time, maximize beam stability, and minimize data size. Due to undersampling, the phase image is pixelated but contains quantitative amplitude and phase information that compares well to the

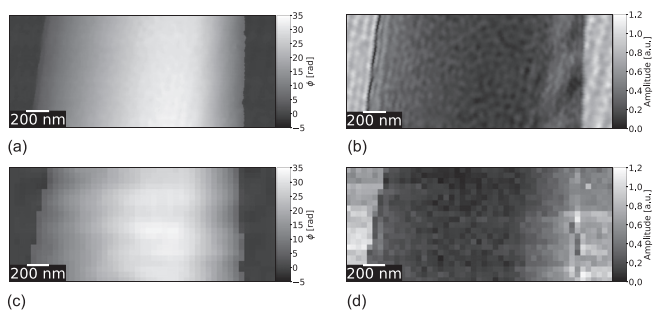


FIG. 3. fSTEMH image of a fabricated Si phase ramp that increases linearly from vacuum with a gradient of $25 \frac{\text{rad}}{\mu\text{m}}$ on one side and decreases linearly with twice the gradient on the other side ($-50 \frac{\text{rad}}{\mu\text{m}}$). (a) and (b) The reconstructed unwrapped phase image as well as the amplitude of the object wave using conventional off-axis electron holography. (c) and (d) Same as (a) and (b), but using fSTEMH with $\Delta x = 5$ μm .

off-axis electron holography reconstruction. Since we were not using a fast-readout detector, the scan time was quite large as each pixel in Figs. 3(c) and 3(d) corresponds to an ≈ 5 s dwell time. The beam current decreased over time, resulting in a decrease in the measured amplitude as seen in Fig. 3(d) from the start of the scan (bottom left) to the end (upper right). This decrease notably does not affect the phase image in Fig. 3(c) and is not present in previous STEMH datasets that utilize a fast readout detector.^{25,26}

In order to determine a range of path separations usable by such an interferometer under these experimental conditions and limit any noise from higher order diffraction probes, we fabricated an aperture with a series of two-slit windows (Fig. S4 in the [supplementary material](#)) with well defined, varied path separations. We used this aperture to isolate p_{+1} and p_{-1} at the specimen plane and measure the fringe visibility \mathcal{V} of the interference fringes at the detector over a range of path separations Δx . We adjusted BP2 to set Δx , BP3 and BP4 to maintain a constant fringe spacing $d_l \approx 147$ μm , and held BP1 = -100 V and all lens values constant throughout. Images of the probes for a selection of path separations and their corresponding averaged, normalized interference fringe profiles are shown in Fig. 4.

The results are shown in Fig. 5. $\mathcal{V}(\Delta x)$ increases until $\Delta x \approx 4$ μm , after which it decreases monotonically. This decrease in \mathcal{V} can be explained by stray magnetic fields passing through the area enclosed by the interferometer. According to the Aharonov-Bohm effect, the phase difference between two paths of an electron interferometer depends linearly on both the area enclosed by the two paths, A , and the time-dependent alternating current (AC) stray magnetic field, $B(t)$. This introduces a time dependent phase in the interference fringes at the detector, modeled as $B(t) = B_0 \sin(\omega t)$.

Here, the interferometer has four enclosed areas. Referring to Fig. 6, A_1 encloses BP2, A_2 is located at the objective lens, A_3 is located at the intermediate 1 lens, and A_4 encloses BP3. This results in four independent phase

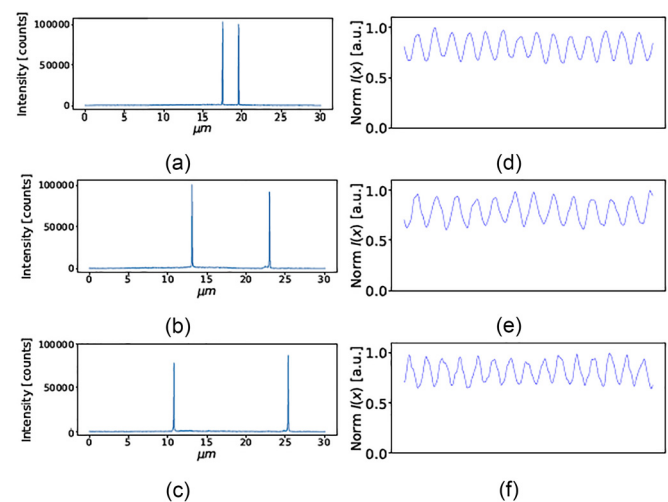


FIG. 4. (a)–(c) 1D profile of p_{+1} and p_{-1} in vacuum with a two slit window aperture inserted in the sample position to block all higher diffraction orders. (d)–(f) Interference fringes acquired over a 10 s exposure for the corresponding path separations shown in (a)–(c).

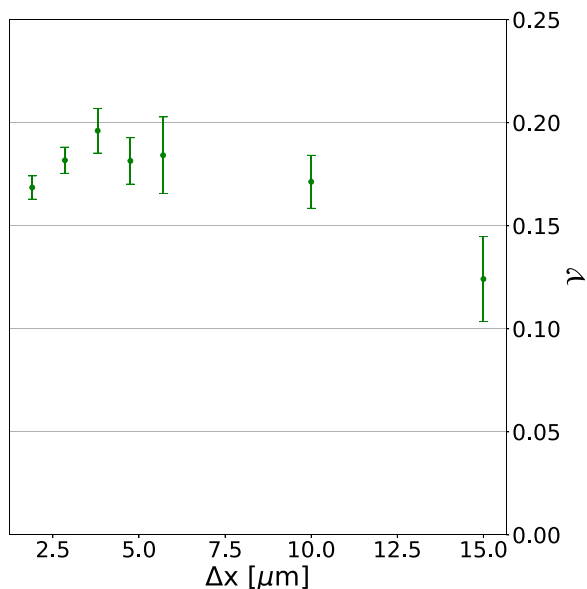


FIG. 5. Interference fringe visibility versus path separation length between the electron probes at the specimen plane.

terms that affect the interference fringes recorded for a finite time interval or 2 s for this experiment.

This time average has a couple of consequences. First, it is a source of noise that decreases the fringe visibility of the interferometer at the onset. Second, increasing A_n increases the amplitude of these phase fluctuations without changing the frequency. When time averaged over the same 2 s time interval, destructive interference decreases the fringe visibility to a minimum.

Initially, BP2 and BP3 are not engaged, and so, the path separation at the Lorentz sample position is $\Delta x = 1.9 \mu\text{m}$. As BP2 is engaged and increased in value, A_1 begins to decrease. We measure an increase in \mathcal{V} for these first changes

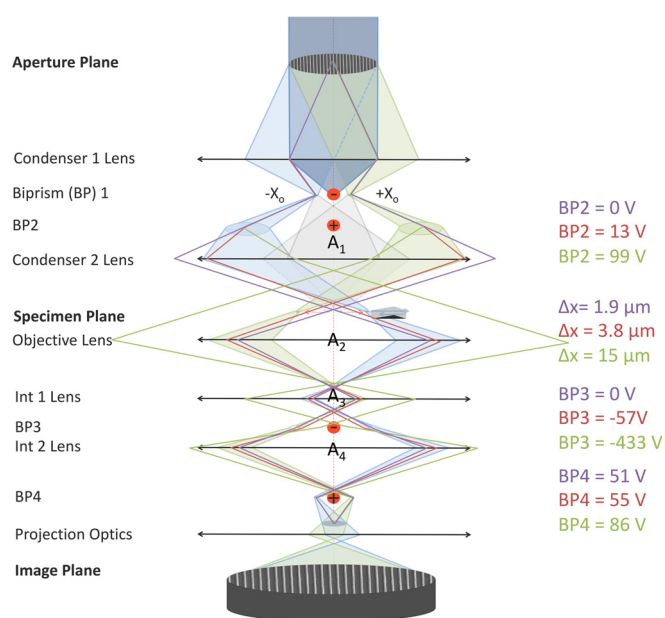


FIG. 6. fSTEMH setup for different path separations. Notice the change in the enclosed areas A_1 , A_2 , A_3 , and A_4 . As the path separation increases initially, the total area enclosed decreases, but then increases monotonically, leading to a loss in fringe visibility for very large path separations.

in BP2, 3, and 4. This could be explained by the stochastic fluctuations of the amplitude and frequency of the thermal magnetic field noise, as described and demonstrated previously by Uhlemann *et al.*²⁹ A_1 is initially large, suggesting that fluctuations in B_1 and ω_1 dominate the phase fluctuations. As A_1 decreases, these phase fluctuations decrease, suggesting that the fringe visibility increases due to more constructive interference over the 2 s exposure. Simultaneously, $A_{n>1}$ all increase in magnitude, suggesting that there must also be an eventual decrease in \mathcal{V} as the path separation increases. This increase in $A_{n>1}$ would explain the decrease in \mathcal{V} for $\Delta x > 3.8 \mu\text{m}$. We simulated this fringe visibility experiment with thermal magnetic field fluctuations and present the results in the [supplementary material](#) in Fig. S3.

To test the largest path separation possible, we increased the path separation to $\Delta x = 25 \mu\text{m}$. However, due to considerations of the voltage that can be applied to BP3 safely, this path separation could only be achieved at a much smaller fringe spacing, $d_f \approx 30 \mu\text{m}$. This spacing corresponds to the Nyquist frequency of the detector, which results in an expected decrease in \mathcal{V} . We measured $\mathcal{V} = 0.67\% \pm 0.15\%$ under these conditions as shown in the [supplementary material](#).

The BPs allow for increased flexibility in multiple ways. The ability to tune the path separation to arbitrarily large values at the specimen plane enables large-geometry electron interferometry experiments. For example, studies of forward-scattering due to atoms or molecules located in an isolated gas cell,³⁰ the nature of the Aharonov-Bohm effect from an isolated solenoid,^{31,32} decoherence theory and the quantum-classical boundary as the delocalized probe entangles with the environment, and enclosing the arms of a charged particle interferometer in a Faraday cage for rotation sensing³³ could all be enabled by this setup. Additionally, fSTEMH may enable quantitative phase mapping with respect to vacuum of programmable phase plates such as the ones proposed by Verbeeck *et al.*³⁴ Each of the above experiments requires either a large spatial separation between interferometer arms in order to place a physical boundary between the two or the ability to tune the path separation over a significant range of values. fSTEMH provides such an interferometric setup.

Furthermore, fSTEMH independently positions the localised reference beam anywhere in a small area of the specimen, whereas conventional TEM holography requires that one wide reference field pass through vacuum outside of the sample, which places limits on the types of specimen geometries that can be imaged. Finally, the use of a holographic beamsplitter allows additional control over the electron beam, such as removing the spherical aberration³⁵ or introducing phase vortices that can be used to measure magnetic fields.³⁶

We demonstrate a tunable path-separated electron interferometer within a STEM. We use a nanofabricated grating as an amplitude-dividing beamsplitter capable of preparing multiple spatially separated, coherent electron probe beams with a 950 nm spatial separation between neighbor diffraction orders at the specimen. We configure four electrostatic bi-prisms (BPs) down the optical column and tune the voltage applied to each to achieve path separations between p_{+1}

and p_{-1} at the specimen plane of up to $25\ \mu\text{m}$ while maintaining fringe visibility at the detector.

We performed fSTEMH on a Si test specimen with the path separation tuned to $5.0\ \mu\text{m}$. We measure highly interpretable, quantitative amplitude and phase contrast that agrees with an independent measurement using off-axis electron holography. We measure the fringe visibility of this interferometer over a range of path separations to establish the interferometer's utility at large path separations. This experimental design can potentially be applied to phase imaging and fundamental physics experiments, such as the Aharonov-Bohm effect, decoherence theory, and electromagnetic field mapping around a specimen's edge without exposing the specimen to radiation.

See [supplementary material](#) for the image of the probes with $\Delta x = 25\ \mu\text{m}$ and the Fourier transform of the corresponding interference fringes, a full analysis of the fringe visibility versus area enclosed by an interferometer including simulations and experimental verification, and an SEM micrograph of the aperture used for the fringe visibility experiment.

The authors wish to thank Jordan Pierce at the University of Oregon for FIB instrument support and instruction. We gratefully acknowledge the use of the RIKEN microscope located at Hitachi, Ltd. in Hatoyama, Japan. Grating fabrication was supported by the U.S. Department of Energy, Office of Science, Basic Energy Sciences, under Award No. DE-SC0010466. F.S.Y. was supported under the National Science Foundation Graduate Research Fellowship Program under Grant No. 1309047 and is a JSPS International Research Fellow.

¹D. Gabor, *Nature* **161**, 777 (1948).

²L. Marton, J. A. Simpson, and J. A. Suddeth, *Phys. Rev.* **90**, 490 (1953).

³G. Möllenstedt and H. Düker, *Naturwissenschaften* **42**, 41 (1955).

⁴G. Matteucci and G. Pozzi, *Ultramicroscopy* **5**, 219 (1980).

⁵G. Pozzi, *Optik* **63**, 227 (1983).

⁶H. Lichte, *Adv Opt. Electron Microsc.* **12**, 25 (1991).

⁷A. Tonomura, *Electron Holography* (Springer-Verlag, Berlin, Heidelberg, 1993).

⁸H. Lichte, D. Geiger, and M. Linck, *Philos. Trans. R. Soc. London A: Math., Phys. Eng. Sci.* **367**, 3773 (2009).

⁹G. Matteucci and G. Pozzi, *Phys. Rev. Lett.* **54**, 2469 (1985).

¹⁰A. Tonomura, N. Osakabe, T. Matsuda, T. Kawasaki, and J. Endo, *Phys. Rev. Lett.* **56**, 792 (1986).

¹¹H. Lichte and M. Lehmann, *Rep. Prog. Phys.* **71**, 016102 (2008).

¹²T. Tanigaki, S. Aizawa, H. S. Park, T. Matsuda, K. Harada, and D. Shindo, *Ultramicroscopy* **137**, 7 (2014).

¹³T. Tanigaki, K. Sato, Z. Akase, S. Aizawa, H. Soon Park, T. Matsuda, Y. Murakami, D. Shindo, and H. Kawase, *Appl. Phys. Lett.* **104**, 131601 (2014).

¹⁴G. Matteucci, G. Missiroli, and G. Pozzi, *Ultramicroscopy* **6**, 109 (1981).

¹⁵Q. Ru, N. Osakabe, J. Endo, and A. Tonomura, *Ultramicroscopy* **53**, 1 (1993).

¹⁶B. McMorrnan and A. Cronin, *Phys. Rev. A* **78**, 013601 (2008).

¹⁷G. Groninger, B. Barwick, H. Batelaan, T. Savas, D. Pritchard, and A. Cronin, *Appl. Phys. Lett.* **87**, 124104 (2005).

¹⁸J. Verbeeck, H. Tian, and P. Schattschneider, *Nature* **467**, 301 (2010).

¹⁹B. J. McMorrnan, A. Agrawal, I. M. Anderson, A. A. Herzing, H. J. Lezec, J. J. McClelland, and J. Unguris, *Science* **331**, 192 (2011).

²⁰T. Harvey, J. Pierce, A. Agrawal, P. Ercius, M. Linck, and B. McMorrnan, *New J. Phys.* **16**, 093039 (2014).

²¹V. Grillo, G. C. Gazzadi, E. Karimi, E. Mafakheri, R. W. Boyd, and S. Frabboni, *Appl. Phys. Lett.* **104**, 043109 (2014).

²²R. Shiloh, Y. Lereah, Y. Lilach, and A. Arie, *Ultramicroscopy* **144**, 26 (2014).

²³F. Yasin, T. Harvey, J. Chess, J. Pierce, and B. McMorrnan, *J. Phys. D: Appl. Phys.* **51**, 205104 (2018).

²⁴A. Caprez, R. Bach, S. McGregor, and H. Batelaan, *J. Phys. B: At., Mol. Opt. Phys.* **42**, 165503 (2009).

²⁵T. Harvey, F. Yasin, J. Chess, J. Pierce, R. dos Reis, P. Özdöl, V. B. Ercius, J. Ciston, W. Feng, N. Kotov, B. McMorrnan, and C. Ophus, preprint [arXiv:1808.00370](#) (2018).

²⁶F. S. Yasin, T. R. Harvey, J. J. Chess, J. S. Pierce, C. Ophus, P. Ercius, and B. J. McMorrnan, *Nano Lett.* **18**, 7118–7123 (2018).

²⁷R. Shiloh, R. Remez, P.-H. Lu, L. Jin, Y. Lereah, A. H. Tavabi, R. E. Dunin-Borkowski, and A. Arie, *Ultramicroscopy* **189**, 46 (2018).

²⁸T. Ohnishi, H. Koike, S. Tomimatsu, K. Umemura, and T. Kamino, in *Proceedings of the 25th International Symposium on Testing and Failure Analysis* (1999), p. 449.

²⁹S. Uhlemann, H. Müller, P. Hartel, J. Zach, and M. Haider, *Phys. Rev. Lett.* **111**, 046101 (2013).

³⁰R. C. Forrey, A. Dalgarno, and J. Schmiedmayer, *Phys. Rev. A* **59**, R942 (1999).

³¹Y. Aharonov and D. Bohm, *Phys. Rev.* **115**, 485 (1959).

³²G. Badurek, H. Weinfurter, R. Ghler, A. Kollmar, S. Wehinger, and A. Zeilinger, *Phys. Rev. Lett.* **71**, 307 (1993).

³³M. Özcan, *J. Appl. Phys.* **83**, 6185 (1998).

³⁴J. Verbeeck, A. Béché, K. Müller-Caspary, G. Guzzinati, M. A. Luong, and M. Den Hertog, *Ultramicroscopy* **190**, 58 (2018).

³⁵M. Linck, P. A. Ercius, J. S. Pierce, and B. J. McMorrnan, *Ultramicroscopy* **182**, 36 (2017).

³⁶V. Grillo, T. R. Harvey, F. Venturi, J. S. Pierce, R. Balboni, F. Bouchard, G. C. Gazzadi, S. Frabboni, A. H. Tavabi, Z.-A. Li, R. E. Dunin-Borkowski, R. W. Boyd, B. J. McMorrnan, and E. Karimi, *Nat. Commun.* **8**, 689 (2017).